

Article

Numerical Modeling of Suspension Force for Bearingless Flywheel Machine Based on Differential Evolution Extreme Learning Machine

Zhiying Zhu ^{1,2,*} , Jin Zhu ¹, Xuan Guo ¹, Yongjiang Jiang ² and Yukun Sun ¹

¹ School of Electric Power Engineering, Nanjing Institute of Technology, Nanjing 211167, China; zhujin_nj@163.com (J.Z.); guoxuannj@163.com (X.G.); syk@njit.edu.cn (Y.S.)

² School of Electrical Engineering, Southeast University, Nanjing 210096, China; jyjzhaoyuan@163.com

* Correspondence: zyzhu@njit.edu.cn; Tel.: +86-181-5100-7500

Received: 25 October 2019; Accepted: 21 November 2019; Published: 23 November 2019



Abstract: The analytical model (AM) of suspension force in a bearingless flywheel machine has model mismatch problems due to magnetic saturation and rotor eccentricity. A numerical modeling method based on the differential evolution (DE) extreme learning machine (ELM) is proposed in this paper. The representative input and output sample set are obtained by finite-element analysis (FEA) and principal component analysis (PCA), and the numerical model of suspension force is obtained by training ELM. Additionally, the DE algorithm is employed to optimize the ELM parameters to improve the model accuracy. Finally, absolute error (AE) and root mean squared error (RMSE) are introduced as evaluation indexes to conduct comparative analyses with other commonly-used machine learning algorithms, such as k-Nearest Neighbor (KNN), the back propagation (BP) algorithm, and support vector machines (SVMs). The results show that, compared with the above algorithm, the proposed method has smaller fitting and prediction errors; the RMSE value is just 22.88% of KNN, 39.90% of BP, and 58.37% of SVM, which verifies the effectiveness and validity of the proposed numerical modeling method.

Keywords: numerical model; principal component analysis; differential evolution; extreme learning machine

1. Introduction

Electric vehicles (EVs) have been researched more and more extensively in recent decades due to problems of energy shortage and environmental pollution. The power battery, as one of the key components of EVs, is extremely important. Compared with chemical batteries, flywheel batteries have relative advantages, such as high power density, rapid charge and discharge, and high cyclic life, as well as being environmentally friendly [1–3]. Bearingless machines with high efficiency and speed and which are friction free are favorable for flywheel batteries [4,5]. Conventional bearingless machines with radial split phase structures can only realize two degrees of freedom (DOF) suspension. Additional radial magnetic bearings are needed to realize radial four DOF active control, which increases the volume and cost, and reduces reliability and effectiveness. The air gap magnetic field of these machines is generated by the current-carrying main windings and suspension windings, so that there are strong electromagnetic coupling characteristics between the suspension force and the electromagnetic torque; as such, it is hard to realize accurate analyses and control [6–8].

Axial split phase bearingless flywheel (ASPBFB) machines can be used in four DOF radial suspension for flywheel rotors by using two phases of suspension windings distributed along the axial direction in one machine. Some effective magnetic isolation measures must be taken to weaken the coupling of

the torque and the suspension control magnetic circuit to reduce the difficulty of analysis and control. This has many advantages, e.g., high integration, low loss, self-decoupling, and easy high-speed control; hence, such technology has broad application prospects in the fields of flywheels and aerospace [9–13].

The establishment of a mathematical model affects the optimal design and performance analysis of the ASPBF machine, and also provides the basis for its high performance control, which is of benefit in terms of the energy storage capacity and operational stability of the flywheel battery; hence, it improves the cruising range of the EVs and stable operation control under various driving situations. However, due to the inherent nonlinearity and magnetic saturation of ASPBF machines, the numerical model of the suspension force is difficult to construct to meet the needs of different modes and complex working conditions. The Maxwell stress tensor method is adopted to build the suspension force under the condition of air gap magnetic density in a saturated, nonlinear state using the classical magnetic saturation correction formula in [14], but the model lacks accuracy due to the fact that many assumptions had to be made. Xiang et al. employed magnetic field energy storage and an equivalent magnetic circuit method to derive the mathematical model of radial force considering eccentric coupling [15]. However, when the current is large, there is a huge error between the calculated value of the mathematical model and the real value, due to magnetic saturation. On the basis of finite element analysis (FEA), Xu et al. obtained a set of mathematical models of suspension force considering magnetic saturation, which has higher levels of accuracy; however, the FEA method affects the rapidity of calculations [16]. Cao et al. combines the rotating coordinate system with the virtual displacement method to establish a mathematical model for conical bearingless machines which can accurately describe the suspension force under the radial and axial displacement of the rotor [17]; however, the method is more complicated to derive, and the key parameters are difficult to obtain. Hence, the analytical modeling (AM) of suspension force in bearingless machines has model mismatch problems due to magnetic saturation and rotor eccentricity.

The extreme learning machine (ELM) is a new learning algorithm for single hidden layer feedforward neural networks. In the execution of the algorithm, it is not necessary to adjust the input weight and hidden layer bias of the network. By simply setting the number of hidden layer nodes in the network, a unique optimal solution can be generated, which has the advantages of fast learning and good generalization performance. In [18,19], a nonparametric model is constructed based on an ELM; compared with traditional neural networks (NNs) and support vector machines (SVMs), it has higher prediction accuracy and computational efficiency. However, since the initial weight and bias are randomly generated, they are not the optimal choices. The resulting model is random, and the accuracy needs to be further improved.

In this paper, a numerical modeling method based on differential evolution (DE) ELM is proposed. Firstly, the topology and working principal of the ASPBF machine are briefly introduced. Next, the basic principles of the related numerical modeling algorithms are described in detail. Then, the FEA method and principal component analysis (PCA) method are used to obtain representative input and output sample data sets. The suspension force numerical model is obtained by training the ELM, and the DE algorithm is used to optimize the key parameters. Finally, compared with the traditional classical algorithm, the results show improvements in the proposed optimal ELM algorithm.

The main contributions of the paper are as follows:

- By employing the advantages of ELM generalization performance and fast learning speed, the numerical model of the suspension force of the machine in magnetic saturation and rotor eccentricity conditions is established, which effectively avoids the low level of precision of the traditional analytical model in the nonlinear region of the machine, as well as the low efficiency of the finite element method.
- Taking the PCA algorithm to reduce the computational dimension of input data in order to ensure data integrity, it is beneficial to reduce the difficulty of solving the ELM optimal weight and offset parameters, which may improve the efficiency and accuracy of the overall model.

- Introducing the DE algorithm with a powerful global search ability to obtain the optimal weight and bias parameters of the ELM, which are beneficial to further realize a high level of precision and rapid modeling of the suspension force of the proposed machine.

The paper is organized as follows: Section 2 includes the topology and working principles of the ASBF machine; Section 3 introduces the proposed new numerical modeling method; Section 4 verifies the superiority and practicability of the proposed modeling method by result comparisons; Section 5 presents the conclusions; and Section 6 discusses future work.

2. Topology and Working Principles

Figure 1 shows the topology of the proposed ASPBF machine. The outer rotor is mounted on the inner side of the flywheel and integrated with the flywheel. The stator and the rotor core are divided into two sections, namely phase A and phase B, according to the phase number in the axial direction, and the axially-magnetized permanent magnet (PM) is arranged between the two-phase stator cores. Each phase adopts an inner stator outer rotor 12/12 pole structure. The inner stator core is divided into a torque pole and a suspension pole. The magnetic isolation sleeve is arranged between the suspension pole and the torque pole to structurally weaken the coupling effect of the torque magnetic circuit and the suspension magnetic circuit.

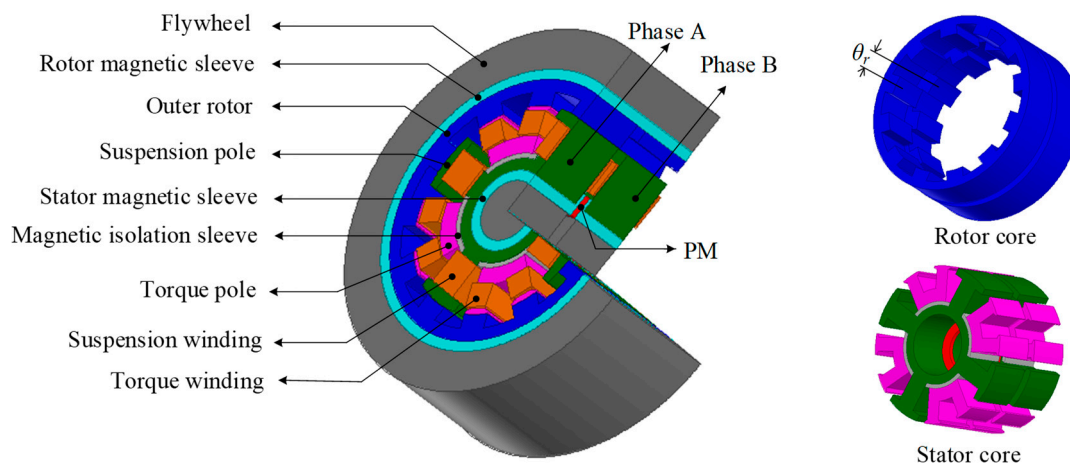


Figure 1. Topology of the proposed ASPBF machine.

Figure 2 shows the magnetic circuit and a cross-section of the machine. It can be seen that the torque control coils and the suspension control coils are stacked on the torque poles and the suspension poles respectively. The control coils on the eight torque poles of each phase are connected in series to form a torque winding to generate a quadrupole torque control magnetic flux Φ_{ma} to drive the rotor, which flows through the torque pole, the air gap, and the outer rotor. The suspension control coils on the two suspension poles are arranged in series to form two sets of suspension windings in an orthogonal direction, and the two-pole suspension control magnetic flux Φ_{sa} generated after energization flows through the suspension pole, the air gap, and the outer rotor. The axially-magnetized PM simultaneously provides a suspension bias magnetic flux Φ_{PM} for the radial four DOF to reduce the suspension power consumption. It flows through the phase A stator sleeve, the phase A suspension pole, the phase A air gap, the phase A rotor, the rotor sleeve, the phase B rotor, the phase B suspension pole, and the phase B stator sleeve. By adjusting the direction of the control flux Φ_{sa} to superimpose or reduce the bias magnetic flux Φ_{PM} , the suspension force required for the four DOF suspension can be generated.

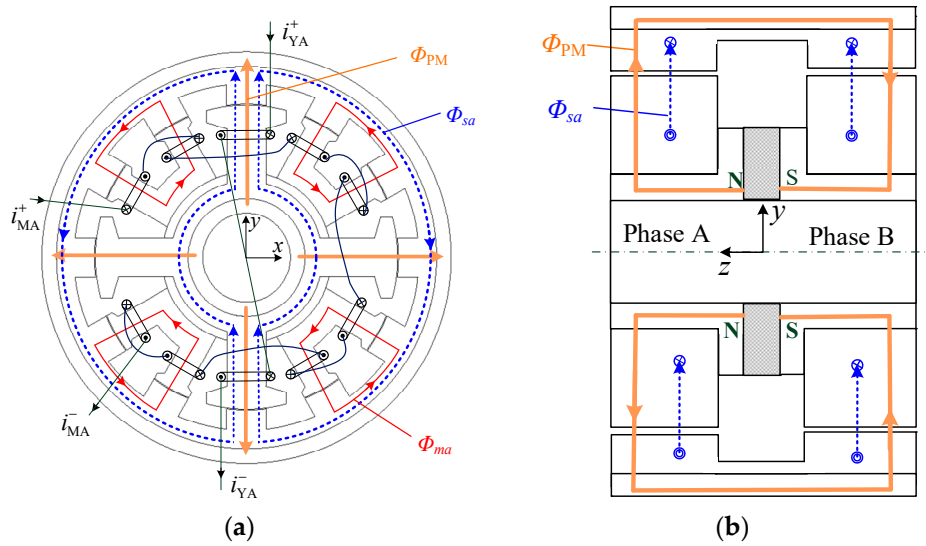


Figure 2. Magnetic circuit and cross-section. (a) Magnetic circuit diagram of radial section; (b) Magnetic circuit diagram of axial section.

When the rotor is in the equilibrium position, there is no current passed through the suspension windings, and no control flux is generated; only the PM generates a bias magnetic flux Φ_{PM} . Due to the symmetry of the machine structure, the air gap length and the bias magnetic flux density between the suspension pole and the rotor are equal, and the rotor will continue to be in equilibrium. Take the machine on the y -axis direction as an example. If the rotor is subjected to a disturbance in the $-y$ direction, the rotor will produce eccentricity in the $-y$ direction, and the magnetic flux generated by PM at the air gap in the $+y$ and $-y$ direction will no longer be equal, which means that the air gap will increase in the $+y$ direction, and the magnetic permeability will decrease; the air gap in the $-y$ direction will decrease, and the magnetic permeability will increase. At this time, radial coils on the y -axis can be controlled to generate a control magnetic flux in the $+y$ direction, superimposed on the bias magnetic flux density of the air gap in the $+y$ direction, and the bias magnetic flux density is weakened at the air gap in the $-y$ direction. Consequently, a radial suspension force in the $+y$ direction is formed, causing the rotor to return to the equilibrium position. The operation principle of the disturbance on the x -axis direction is similar. The superposition of the force on the x - and y -axes can generate a suspension force in any direction, thereby achieving the suspension of the four DOF of the rotor.

The equivalent magnetic circuit of the suspension system includes a bias magnetic circuit and a control magnetic circuit. In order to simplify the calculation of the magnetic circuit, the following assumptions are made on the equivalent magnetic circuit of the suspension system: Only the leakage magnetic flux of the inner and outer surfaces of the permanent magnet is considered, and the whole magnetic circuit system is regarded as a system in which magnetic leakage reluctance is connected in parallel with the effective magnetic circuit; And finally, a PM is used to provide a bias magnetic flux, and only the magnetic reluctance of the working air gap is considered, while the core magnetoresistance, rotor magnetoresistance, and eddy current loss are ignored. Figure 3 shows the equivalent magnetic circuit of the suspension system. In the figure, F_{PM} is the magnetomotive force of the PM, R_{PM} is the magnetic reluctance of the PM, Φ_{PM} is the magnetic flux of the PM, N is the number of the suspension winding, i_{Ax} , i_{Ay} , i_{Bx} , i_{By} are the control currents of the suspending windings of phase A and B respectively. R_{Ax}^+ , R_{Ax}^- , R_{Ay}^+ , R_{Ay}^- are the air gap reluctance of the phase A, R_{Bx}^+ , R_{Bx}^- , R_{By}^+ , R_{By}^- are the air gap reluctance of phase B, Φ_{PMAx}^+ , Φ_{PMAx}^- , Φ_{PMAy}^+ , Φ_{PMAy}^- are the bias magnetic fluxes of air gap of phase A, Φ_{PMBx}^+ , Φ_{PMBx}^- , Φ_{PMBy}^+ , Φ_{PMBy}^- are the bias magnetic fluxes of air gap of phase B, Φ_{SAx}^+ , Φ_{SAx}^- , Φ_{SAy}^+ , Φ_{SAy}^- are the control magnetic fluxes of phase A, and Φ_{SBx}^+ , Φ_{SBx}^- , Φ_{SBy}^+ , Φ_{SBy}^- are the control magnetic fluxes of phase B.

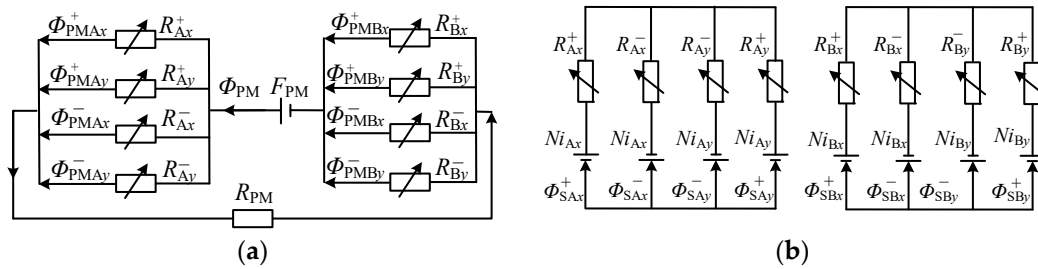


Figure 3. Equivalent magnetic circuit of the suspension system. (a) Bias magnetic circuit; (b) Suspension pole control magnetic circuit of Phase A and Phase B.

Due to the symmetry of the two-phase structure of A and B, the x -direction eccentricity of the phase A rotor is taken as an example for analysis in the following calculations. Assuming that the eccentricity of the rotor in $-x$ direction is x , the reluctance at each air gap is

$$\begin{cases} R_{Ax}^+ = \frac{gl+x}{\mu_0 S} & R_{Ax}^- = \frac{gl-x}{\mu_0 S} \\ R_{Ay}^+ = R_{Ay}^- = \frac{gl}{\mu_0 S} \end{cases} \quad (1)$$

where μ_0 is the air permeability at the air gap, gl is the air gap length between the stator and the rotor, S is the magnetic flux area of each magnetic pole, and x is the offset distance of the rotor in $-x$ direction.

According to the magnetic path Kirchhoff's law, the bias magnetic flux at each air gap in the x -direction can be obtained as

$$\begin{cases} \Phi_{PMAx}^+ = \frac{F_{PM}}{(R_{PM}+2/P)\sigma} \cdot \frac{1}{R_{Ax}^+ P} \\ \Phi_{PMAx}^- = \frac{F_{PM}}{(R_{PM}+2/P)\sigma} \cdot \frac{1}{R_{Ax}^- P} \end{cases} \quad (2)$$

where $F_{PM} = L_{PM}H_c$, L_{PM} is the axial magnetization length of the PM and H_c is the coercivity coefficient. σ is the magnetic flux leakage coefficient of the PM, $P = \frac{1}{R_{Ax}^+} + \frac{1}{R_{Ax}^-} + \frac{1}{R_{Bx}^+} + \frac{1}{R_{Bx}^-}$.

After a control current is applied in the x -direction, the control flux at each air gap is

$$\begin{cases} \Phi_{SAx}^+ = \frac{Ni_{Ax}}{R_1} + \frac{Ni_{Ax}}{R_2} \cdot \frac{R_2 - R_{Ax}^-}{R_{Ax}^+} \\ \Phi_{SAx}^- = \frac{Ni_{Ax}}{R_2} + \frac{Ni_{Ax}}{R_1} \cdot \frac{R_1 - R_{Ax}^+}{R_{Ax}^-} \end{cases} \quad (3)$$

where R_1 and R_2 are defined as

$$\begin{cases} R_1 = R_{Ax}^+ + \frac{1}{\frac{1}{R_{Ax}^-} + \frac{1}{R_{Ay}^+} + \frac{1}{R_{Ay}^-}} \\ R_2 = R_{Ax}^- + \frac{1}{\frac{1}{R_{Ax}^+} + \frac{1}{R_{Ay}^+} + \frac{1}{R_{Ay}^-}} \end{cases} \quad (4)$$

Based on the above magnetic circuit, according to the Maxwell stress method, the formula for calculating the radial suspension force on the x -axis of the system is summarized in Equation (5).

$$F_{Ax} = \frac{(\Phi_{SAx}^+ + \Phi_{PMAx}^+)^2 - (\Phi_{SAx}^- - \Phi_{PMAx}^+)^2}{2\mu_0 S} \quad (5)$$

As shown in Equations (1)–(5), the model of suspension force for ASPBF deduced by AM clearly indicates the relationships between machine performance and the corresponding structural parameters. Nevertheless, given the existence of ideal assumptions, the calculation model obtained by the AM can't get a good fit in the condition of nonlinearity and magnetic saturation of bearingless machines, which means that it is difficult to achieve accuracy under different modes and complex working conditions.

3. Proposed New Numerical Modeling Method

3.1. ELM Prediction Model

ELM is an effective single hidden layer, feedforward, neural network learning algorithm proposed by G. Huang [20]. The schematic diagram of the ELM is shown in Figure 4.

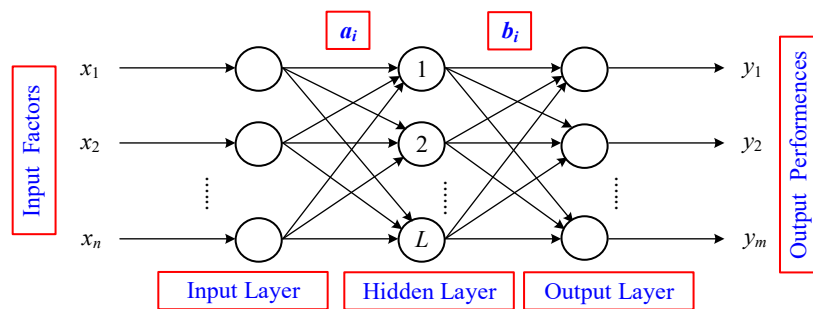


Figure 4. Schematic diagram of the ELM.

For N_a arbitrary samples, where $x_i = [x_{i1}, x_{i2}, \dots, x_{in}]^T \in R^n$, $y_i = [y_{i1}, y_{i2}, \dots, y_{im}]^T \in R^m$, the output of a feedforward neural network with L hidden layer nodes and the excitation function $G(x)$ can be expressed as follows:

$$f_L(x) = \sum_{i=1}^L \beta_i G(a_i \cdot x_i + b_i) \quad (6)$$

where $a_i = [a_{i1}, a_{i2}, \dots, a_{in}]^T$, which is the input weight of the input layer to the i -th hidden layer node, $x_i \in R^n$, $a_i \in R^n$, $\beta_i \in R^m$, b_i is the bias of the i -th hidden layer node, $\beta_i = [\beta_{i1}, \beta_{i2}, \dots, \beta_{im}]^T$ is the output weight of the i -th hidden layer node, $a_i \cdot x_i$ represents the inner product of vectors a_i and x_i , and the excitation function $G(x)$ can select "Sigmoid", "Sine", or "RBF", etc. If the feedforward neural network with L hidden layer nodes can approximate the N samples with zero error, then a_i , b_i , and β_i satisfy the following equation:

$$f_L(x) = \sum_{i=1}^L \beta_i G(a_i \cdot x_j + b_i), j = 1, \dots, N_a \quad (7)$$

Equation (7) can be simplified to

$$H\beta = Y \quad (8)$$

where Y is the desired output matrix, β is the output weight matrix, and H is the hidden layer output matrix of the network, described as follows:

$$\begin{bmatrix} G(a_1 \cdot x_1 + b_1) & \cdots & G(a_L \cdot x_1 + b_L) \\ \vdots & G(a_i \cdot x_j + b_i) & \vdots \\ G(a_1 \cdot x_N + b_1) & \cdots & G(a_L \cdot x_N + b_L) \end{bmatrix}_{N \times L} \quad (9)$$

In the ELM algorithm, since the output weight and the hidden layer bias are given randomly, the hidden layer matrix H becomes a certain matrix. Such a feedforward neural network is transformed into a problem of solving the least squares solution of the output weight matrix, which means that the network training can be completed. The output weight matrix β can be obtained with Equation (10):

$$\beta = H^+ Y \quad (10)$$

where H^+ represents the Moore-Penrose generalized inverse of the hidden layer output matrix H .

3.2. Differential Evolution Algorithm

The DE algorithm is a new group, intelligent optimization algorithm based on population iteration, which uses a simple differential mutation operator and a survival-of-the-fittest strategy to generate new populations, and finally, enables the population to reach or approach the global optimal solution of the optimization problem. It has the advantages of fast convergence, fewer adjustable parameters, and good robustness [21]. A flow chart of the DE algorithm is shown in Figure 5; the specific steps are as follows:

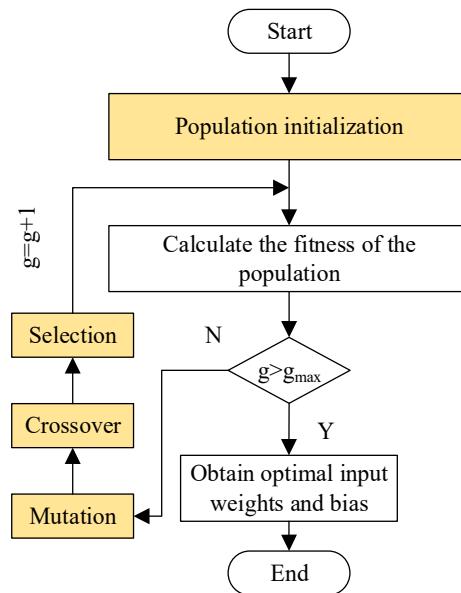


Figure 5. Flow chart of the DE algorithm.

Step 1—Population initialization: randomly select individual P (satisfying the constraints) and form a population of size N_p . The i -th individual P_i is formed as follows:

$$P_i = \{P_{i1}, P_{i2}, \dots, P_{ij}, \dots, P_{iD}\} \quad j = 1, 2, \dots, D \quad (11)$$

where $i = 1, 2, \dots, N_p$, D is the number of genes on an individual, P_{ij} represents the j -th gene on the i -th individual, and $P_{ij} = \text{rand}(0, 1) \cdot (P_{ij}^U - P_{ij}^L) + P_{ij}^L$, $\text{rand}(0, 1)$ is a random integer between $(0, 1)$, while P_{ij}^U and P_{ij}^L are the upper and lower limits of the j -th gene on the i -th individual, respectively.

Step 2—Mutation operation: randomly select three unequal individuals $(P_{r1,g}, P_{r2,g}, P_{r3,g})$ from the population and mutate according to Formula (12):

$$v_{r,g+1} = p_{r1,g} + F(p_{r2,g} - p_{r3,g}) \quad (12)$$

where g represents the current generation, $P_{r1,g}$, $P_{r2,g}$ and $P_{r3,g}$ are the $r1$ -th, $r2$ -th, and $r3$ -th individual in the g -th generation respectively, and $r_1 \neq r_2 \neq r_3 \neq r$. $v_{r,g+1}$ is a newly-constructed vector in the next generation, while F is the scaling factor.

Step 3—Crossover operation: the new individual $v_{r,g+1}$, obtained by mutation, and the parent P_i are discretely crossed to obtain the updated individual u_i :

$$u_{ij,g+1} = \begin{cases} v_{ij,g+1} & \text{rand}(0, 1) \leq CR \parallel j = \text{rand}(1, D) \\ P_{ij,g} & \text{otherwise} \end{cases} \quad (13)$$

where CR is the crossover probability, $\text{rand}(1,D)$ is a random integer between $(1,D)$, and j represents the j -th gene on an individual.

Step4—Selection operation: the fitness values of individuals in the new previous generation are compared, and the individuals with smaller value will enter the next generation; otherwise, they retain:

$$p_{i,g+1} = \begin{cases} u_{i,g+1} & f(u_{i,g+1}) \leq f(p_{i,g}) \\ p_{i,g} & \text{otherwise} \end{cases} \quad (14)$$

where $f(\cdot)$ is the selected fitness function.

Repeat the above mutation, crossover, and selection process until the maximum number of iterations g_{\max} and the output can get the optimal input weight and hidden layer bias matrix combination of the ELM network.

3.3. Numerical Simulation of Suspension Force Based on DE Optimized ELM

Although ELM can realize nonlinear function fitting and prediction problems with small sample learning, it has been shown that the input weight a_i and hidden layer bias b_i of ELM determine the performance of the model. In order to realize high-precision and rapid modeling of the proposed suspension force model, the powerful global search ability of the DE algorithm is used to automatically optimize the parameters a_i and b_i to seek the best modeling and prediction effects.

For the parameters that ELM needs to optimize, the root mean square error (RMSE) of the actual value and the model prediction value is selected as the fitness function of the differential evolution algorithm. The expression is as follows:

$$\text{RMSE} = \sqrt{\frac{1}{N} \sum_{i=1}^N (y_i - \hat{y}_i)^2}, \quad i = 1, 2, \dots, N_t \quad (15)$$

where y_i and \hat{y}_i are the actual and predicted values of the suspension force respectively, and N_t is the total number of training samples.

As shown in Figure 6, the numerical modeling method of suspension force for the proposed machine based on DE optimized ELM comprises four specific steps, as follows:

Step 1—Collect representative input and output data for variables. In this paper, the FEA is used to obtain the suspension force characteristics under different working conditions such as magnetic saturation and rotor eccentric. The radial eccentricity x and y , the suspension winding current i , and the rotor position θ are selected as the parameter variables of the FEA model to calculate the performance characteristics of the machine, e.g., the suspension output F with a combination of these parameters.

Step 2—Pretreat data set with the PCA algorithm, establish the principal input components Z_i , and output the F sample set for training and testing the ELM model.

Step 3—Optimize the weight and hidden layer bias of ELM by means of DE algorithm to obtain the optimal ELM.

Step 4—By training the ELM with the optimal weight and hidden layer bias based on the data set after dimension reduction, the numerical model of suspension force will be obtained.

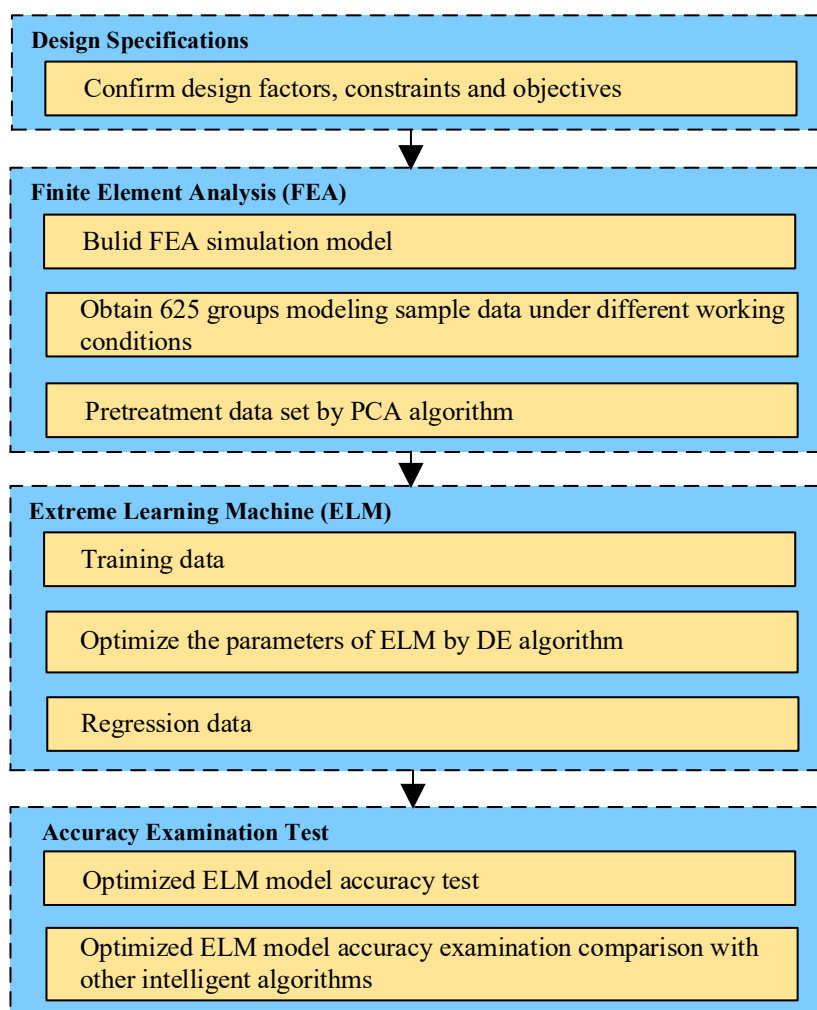


Figure 6. Diagram of the DE optimized ELM modeling method.

4. Comparison and Analysis of Results

4.1. Acquisition and Processing of Modeling Data

A three-dimensional FEA model of the proposed machine was constructed to get the corresponding simulation results using a combination of four parameters, i.e., x , y , i and θ . The values and step sizes of these parameters are shown in Table 1. The mesh grid and the magnetic field intensity distribution of FEA are illustrated in Figure 7. As shown in Table 1, the four parameters have five levels, which results in $5^4 = 625$ combinations of initial sample data sets under different combinations. Considering that under different working conditions, the torque performance T will also have an impact on the suspension force of the machine, we additionally select the torque T as the input data of the ELM training, which means that during the modeling operation, factors including x , y , i , θ , and T are selected as the input components, and the radial suspension force F is employed as the output component for ELM regression training. Table 2 shows the initial sample data set for ELM regression.

Table 1. Input parameter value ranges and step sizes.

Parameters	Value Ranges	Step Sizes
Rotor position θ ($^\circ$)	6~30	6
x -axis radial eccentricity x (mm)	0.02~0.1	0.02
y -axis radial eccentricity y (mm)	0.02~0.1	0.02
Suspension winding current i (A)	0.2~1	0.2

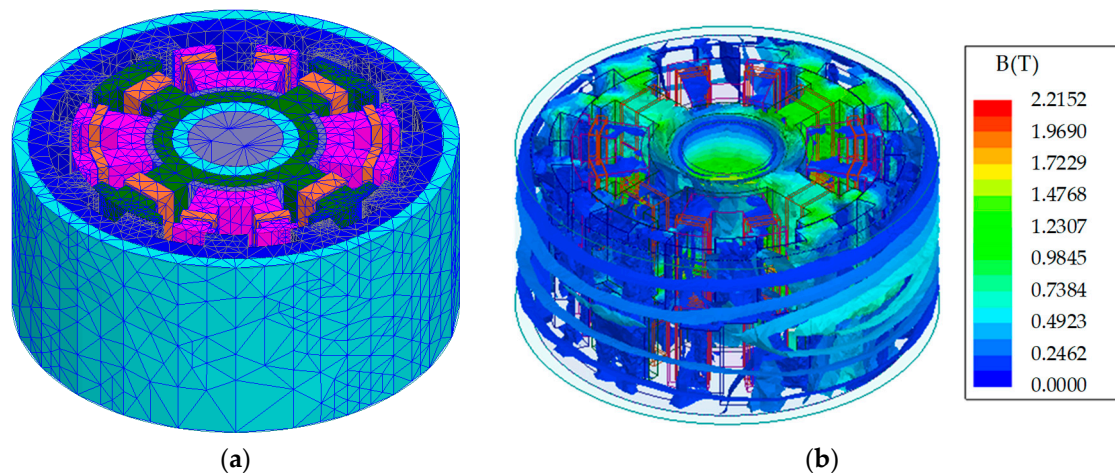


Figure 7. Three-dimensional FEA model of the proposed machine. (a) Mesh grid of FEA; (b) Magnetic field intensity distribution.

Table 2. Initial sample data set for ELM regression.

NO.	Inputs				Outputs	
	x (mm)	y (mm)	i (A)	θ ($^{\circ}$)	T (mN·m)	F (N)
1	0.02	0.02	0.2	6	141.21	30.60
2	0.04	0.02	0.2	6	166.30	33.58
3	0.06	0.02	0.2	6	167.59	40.69
...
623	0.06	0.10	1.0	30	-100.78	125.67
624	0.08	0.10	1.0	30	-121.59	134.47
625	0.10	0.10	1.0	30	-119.63	150.80

Considering the influence of redundancy and correlation between multivariate components on the accuracy of the model, the PCA method is used to reduce the dimension and filter the sample dataset obtained using a finite element simulation to improve the accuracy and efficiency of the modeling.

Through operations of PCA, the contribution rate of each component after the dimension reduction process is shown from high to low in Table 3. In Table 3, it can be seen that the cumulative contribution rate of the first four components (Z_1 , Z_2 , Z_3 , and Z_4) in the new low-dimensional space has reached 88.1%, which means these components have greatly preserved the information carried by the original data, and the influence of the last component is relatively negligible. Therefore, the data set (Z_1 , Z_2 , Z_3 , and Z_4) is selected after dimension reduction, as the input set and F is the output set to train the DE optimized ELM to eliminate redundancy between related variables.

Table 3. Contribution rate of each component.

Component	Covariance Matrix Eigenvalue λ	Contribution Rate (%)	Cumulative Contribution Rate (%)
Z_1	0.6222	26.4665	26.4665
Z_2	0.5012	21.3195	47.7860
Z_3	0.5009	21.3067	69.0927
Z_4	0.4468	19.0055	88.0982
Z_5	0.2798	11.9018	100

After the pretreatment of PCA, the computational dimension of the input data is reduced by 20% without losing the data integrity, which may reduce the difficulty of solving the optimal weight and bias parameters of the ELM and improve the efficiency and accuracy of the overall training of the model. The data after dimension reduction is shown in Table 4.

Table 4. Data set after dimension reduction.

No.	Principal Components				Outputs
	Z ₁	Z ₂	Z ₃	Z ₄	F (N)
1	−0.5162	−0.2318	−1.4044	−1.3090	30.60
2	−0.5636	0.1559	−1.0949	−1.3859	33.58
3	−0.5494	0.5468	−0.7854	−1.4173	40.69
...
...
623	0.9548	−0.6301	0.7854	0.6190	125.67
624	1.0183	−0.2367	1.0949	0.6239	134.47
625	1.0348	0.1543	1.4044	0.5941	150.80

4.2. Comparison of Prediction Performance of ELM Algorithm Before and After Optimization

The 625 sets of data after dimension reduction in Table 4 are divided into two groups according to the steps described in Part 3.3, wherein 525 sets of data are training sets which are used to determine the input weight and hidden layer bias of the numerical model, while the remaining 50 sets are used as test sets to verify the accuracy of the predicted values of the ELM model. In order to verify the effectiveness of the proposed DE optimized ELM algorithm, this paper uses the same training and testing set data to perform regression analyses on the PCA-ELM algorithm and the proposed optimized ELM algorithm, and compares them with the predicted values obtained by the conventional ELM algorithm under the same 625 data sets. In order to further explain the accuracy of the prediction model built using the DE algorithm, the RMSE of the predicted values is introduced as the evaluation index. The RMSE definition is as shown in Equation (15).

Figure 8 shows the comparison curves of the three numerical models of the conventional ELM, PCA-ELM, and the proposed optimized ELM. Table 5 shows RMSE values of the predicted and actual suspension force obtained by the three methods. Combined with Figure 8 and Table 5, we can clearly see that the conventional ELM model has a low degree of accuracy, and that the RMSE reaches 12.5643, which means that it is unlikely that it will be able to meet the requirements of subsequent suspension control in spite of its short calculation time. Preprocessed using the PCA algorithm, the computing cost and accuracy of the PCA-ELM model are slightly improved, but due to the randomness of the weight and bias parameters of the ELM network, the improvement is insignificant. Compared with the former two, the proposed optimal ELM combines the advantages of PCA and conventional ELM algorithms, and introduces the DE algorithm to obtain the optimal weight and bias parameters of the neural network, which has higher prediction accuracy. The RMSE value is 4.2907, only 34.15% of conventional ELM and 38.76% of the PCA-ELM, which demonstrates the accuracy and effectiveness of this algorithm.

Table 5. Comparison of three numerical models in RMSE value.

Models	RMSE
ELM	12.5643
PCA-ELM	11.0689
Proposed optimal ELM	4.2907

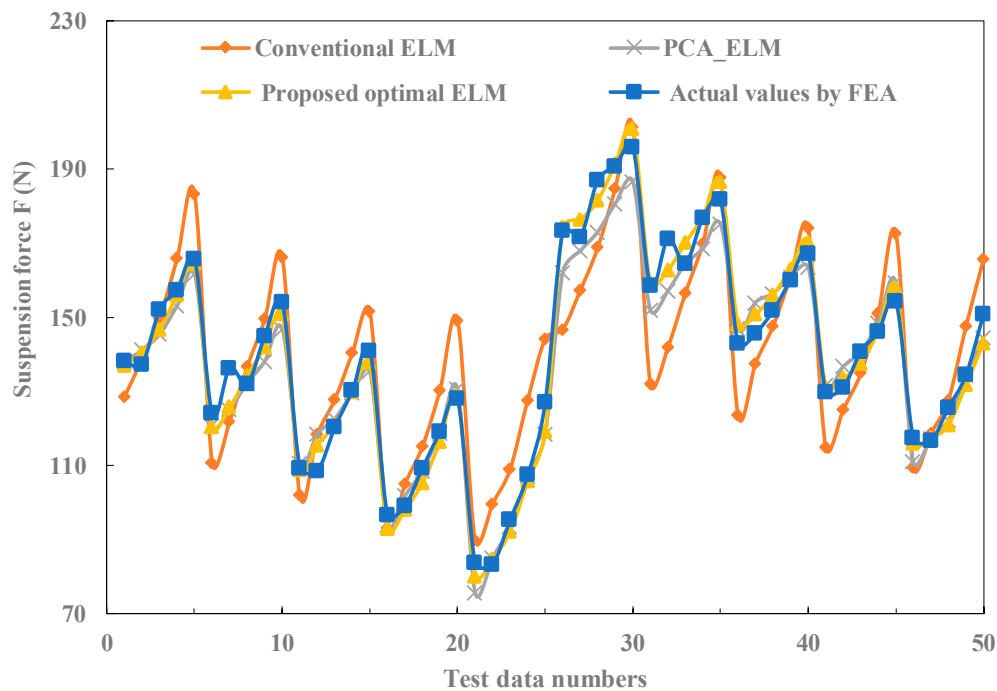


Figure 8. Prediction effect comparison of three numerical model.

4.3. Comparison of Prediction Performance of Four Different Algorithms

In order to further illustrate the effectiveness of the proposed algorithm, other commonly-used machine learning algorithms such as k-Nearest Neighbor (KNN), the back propagation (BP) algorithm, and support vector machines (SVMs) are introduced for comparative analyses [22–28]. In the development of the predictive model, the key parameters of each algorithm are set as follows:

- KNN:** the nearest neighbor number K in the KNN algorithm is 5, and the distance calculation method is selected as the Euclidean distance.
- BP:** The number of iterations of the BP algorithm network is 500, the learning rate is set at 0.1, and the learning goal is 0.001.
- SVM:** The Matlab package *libsvm* (v.3.22) is taken to implement SVM. We choose the radial basis function (RBF) as the kernel function of SVM because the actual operation results have shown that RBF performed better than the other three kernel functions (linear, polynomial, and sigmoid). In addition, the grid search method is also employed to establish the search space of two key parameters in the RBF-SVM, i.e., the penalty parameter C and the kernel parameter γ . The search space and step size are as follows:

$$\begin{cases} 2^{-9} \leq C \leq 2^9 & \text{with step } \Delta C = 0.5 \\ 2^{-9} \leq \gamma \leq 2^9 & \text{with step } \Delta \gamma = 0.5 \end{cases} \quad (16)$$

- Proposed optimal ELM:** The number of hidden layer nodes L is set to 35, the population size N_p is taken as 30, the scaling factor F is 0.7, the crossover probability CR is selected as 0.8, and the maximum number of iterations g_{\max} is set to 110.

Generally, three cross-validation methods, namely the hold-out method, a K-fold cross-validation (K-CV), and a leave-one-out cross-validation (LOO-CV) test, are often used to evaluate the regression accuracy of the model [29,30]. In this study, the hold-out method is selected to verify the prediction accuracy of each model. During the hold-out method, all data sets are divided into two groups, i.e., training sets and testing sets, and each algorithm makes use of the same 575 sets of data after dimension reduction as the training set and the remaining independent 50 sets of data for accuracy testing. At the

same time, the RMSE and the absolute error (AE) of the predicted value and the actual value are also introduced as evaluation indexes to further evaluate each prediction model. AE is defined as

$$AE = |y_i - \hat{y}_i|, \quad i = 1, 2, \dots, N_t \quad (17)$$

where y_i and \hat{y}_i are the actual and predicted values of the suspension force respectively, and N_t is the total number of training samples.

The final fitting and prediction results are shown in Figures 9 and 10 (the 50 sets of data shown by the fitting error in Figure 9 are randomly selected from the corresponding results from 525 sets of training set data by different algorithms), and the computing time and RMSE of the predicted and actual values are shown in Table 6. Taking the AE index as an example, and comparing the four images in Figure 9, we can clearly find that proposed optimal ELM model has smaller fitting and fewer prediction errors than the classical KNN, BP, and SVM algorithms, and that the data distribution is more stable and denser. In addition, taking Figure 10 and Table 6 into account, it can be seen that the proposed optimal ELM has the highest modeling accuracy among the four aforementioned algorithms. The computing time of the proposed optimal ELM is 17.0053 s, which is 40.66% of the SVM algorithm, but the prediction error in the RMSE value is 58.37% of the SVM. The computing times of KNN and BP are smaller than the proposed optimal ELM; however, the models of KNN and BP are of the most inaccurate, yielding 18.7541 and 10.7538, which is more than 2.5 times the prediction error of the ELM. Hence, it can be seen that the optimal ELM algorithm can effectively improve the fitting and prediction accuracy of the model, as does the computing efficiency of the model.

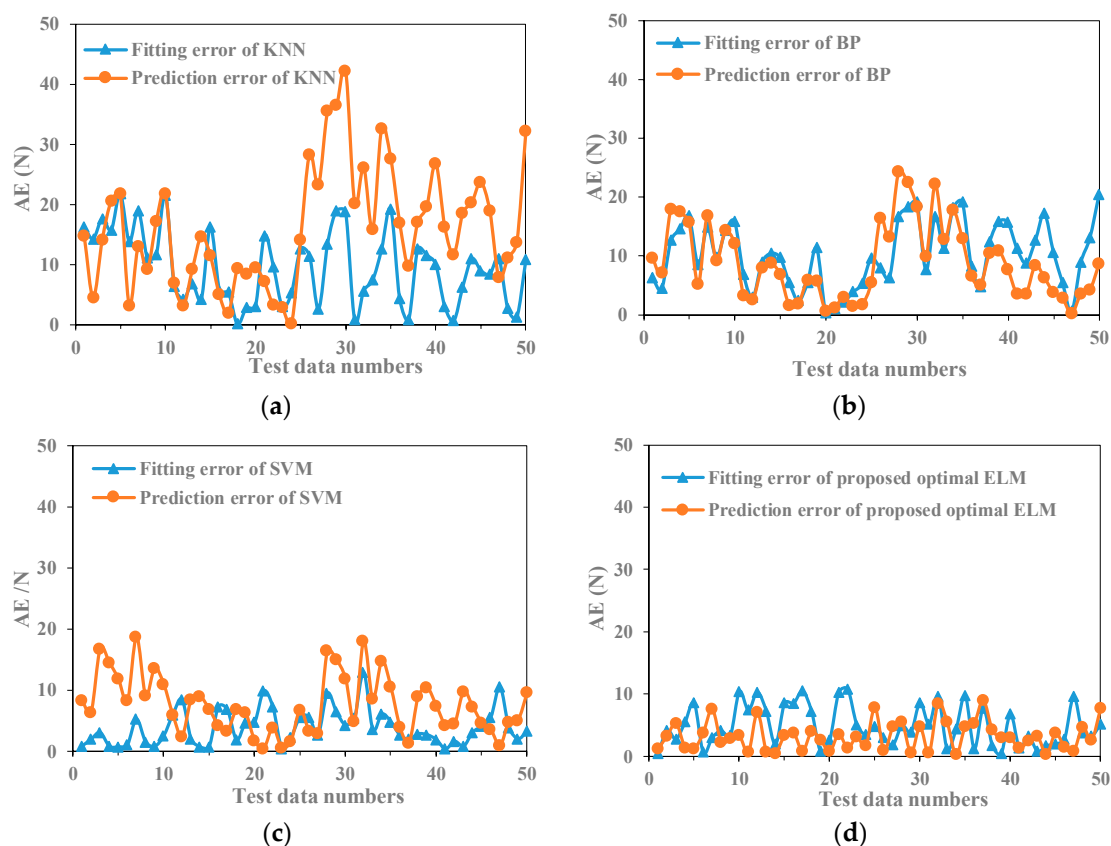


Figure 9. Comparison of four algorithms on fitting and prediction errors. (a) Obtained by the KNN; (b) Obtained by the BP; (c) Obtained by the SVM; (d) Obtained by the proposed optimal ELM.

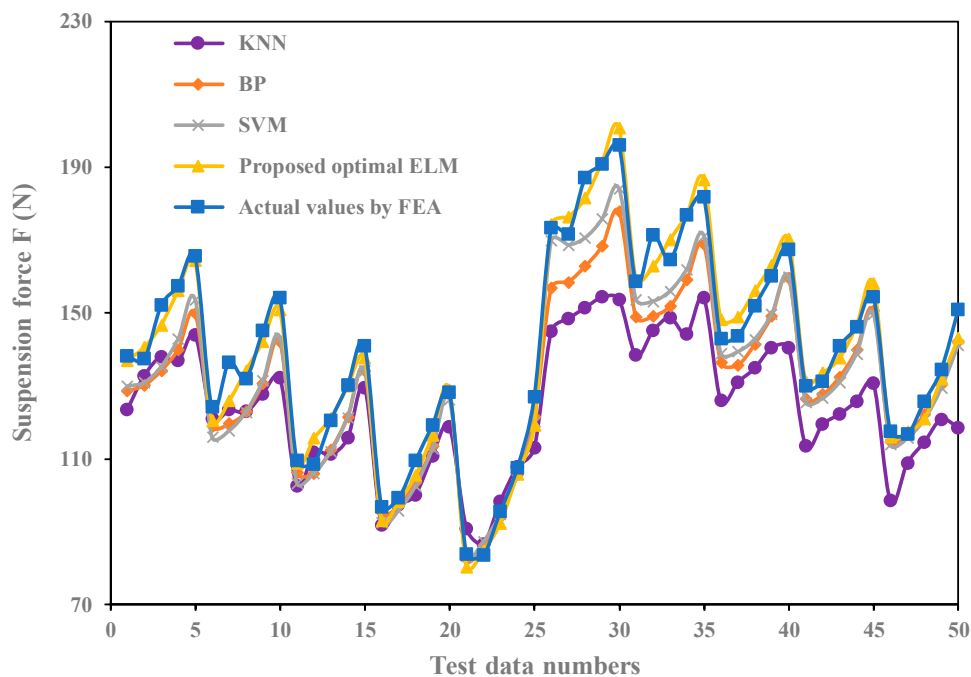


Figure 10. Comparison of four algorithms on prediction effects.

Table 6. Comparison of four algorithms in RMSE value and computing time.

Models	RMSE	Computing Time (s)
KNN	18.7541	0.39429
BP	10.7538	0.8047
SVM	7.3510	41.8263
Proposed optimal ELM	4.2907	17.0053

5. Conclusions

A numerical model of suspension force for an ASPBF machine was constructed using the optimal ELM algorithm. The suspension characteristics under magnetic saturation and rotor eccentricity were obtained by dimensional FEA model, which can provide an effective learning sample set for the ELM model. Additionally, the DE algorithm, adopted to optimize the parameters of ELM, can avoid the blindness of artificial selection and significantly enhance the prediction accuracy of the model.

6. Discussion

Combined with the results of the research in this paper, the authors aim to perform the following research in the future:

- (1) Expand the range of values of the existing design parameters (x, y, i, θ) to establish a numerical model of the levitation force of the proposed machine under high current, large eccentricity, and full cycle, so as to explore whether the method described in this paper has a strong generalization ability and practical application prospects, and whether it can further satisfy the accurate modeling of the suspension force under the condition of the multivariable working conditions of the actual operation of the machine.
- (2) Select more design parameters to verify the proposed modeling method. From Equations (1)–(5), the performance of the machine suspension force is greatly affected by the machine winding current and magnetoresistance. However, this paper only studies the radial eccentricity of the machine, that is, the length of the air gap reluctance and the influence of the suspension winding current. Next, more design parameters will be studied to further verify the effectiveness of

the proposed modeling method. Other design parameters include the torque winding current, the permanent magnet internal diameter, the suspension pole arc, the rotor pole arc, etc.

- (3) Improve the efficiency of modeling data acquisition. The author will further combine other experimental design methods, such as the Taguchi method, the response surface method, etc., to scientifically arrange the experimental parameters to (i) ensure a reduction of the number of finite element calculations based on the integrity of the data, (ii) improve the efficiency of the simulation calculation, and (iii) effectively shorten the period of the numerical modeling process globally.

Author Contributions: Z.Z. contributed to the numerical modeling method and optimization framework; J.Z. collected the data and built the models; X.G. and Y.J. contributed to the FEA and analytical model. Y.S. contributed to the application and provided helpful advice. J.Z. wrote the paper and Z.Z. reviewed and edited the paper.

Funding: This research was funded by the National Natural Science Foundation of China (51977103, 51877101), the Postdoctoral Science Foundation Funded Project of China (2018M632201), the Six Talent Peaks Project of Jiangsu (GDZB-026), the Postgraduate Research & Practice Innovation Program of Jiangsu Province (SJCX18_0565, SJCX19_0525) and the College Students Science and Technology Innovation Fund of Nanjing Institute of Technology (TZ20190031).

Acknowledgments: The authors are thankful to anonymous reviewers for their valuable comments on this paper.

Conflicts of Interest: The authors declare no conflict of interest.

Nomenclature

Symbol	Meaning
Φ_{ma}	torque control magnetic flux
Φ_{sa}	suspension control magnetic flux
Φ_{PM}	suspension bias magnetic flux
F_{PM}	magnetomotive force of permanent magnet
R_{PM}	magnetic reluctance of permanent magnet
N	number of the suspension winding
$i_{Ax'}, i_{Ay'}, i_{Bx'}, i_{By'}$	control currents of the suspending windings of phase A and B
$R_{Ax}^+, R_{Ax}^-, R_{Ay}^+, R_{Ay}^-$	air gap reluctance of the phase A
$R_{Bx}^+, R_{Bx}^-, R_{By}^+, R_{By}^-$	air gap reluctance of the phase B
$\Phi_{PMAx}^+, \Phi_{PMAx}^-, \Phi_{PMAy}^+, \Phi_{PMAy}^-$	bias magnetic fluxes of the air gap of phase A
$\Phi_{PMBx}^+, \Phi_{PMBx}^-, \Phi_{PMBy}^+, \Phi_{PMBy}^-$	bias magnetic fluxes of the air gap of phase B
$\Phi_{SAx}^+, \Phi_{SAx}^-, \Phi_{SAy}^+, \Phi_{SAy}^-$	control magnetic fluxes of phase A
$\Phi_{SBx}^+, \Phi_{SBx}^-, \Phi_{SBy}^+, \Phi_{SBy}^-$	control magnetic fluxes of phase B
μ_0	air permeability
g_l	air gap length between the stator and the rotor
S	magnetic flux area of each magnetic pole
x, y	offset distance of the rotor in x,y direction
L_{PM}	axial magnetization length of permanent magnet
H_c	coercivity coefficient
σ	magnetic flux leakage coefficient of permanent magnet
L	number of hidden layer nodes in ELM
$G(x)$	excitation function of ELM
$a_i = [a_{i1}, a_{i2}, \dots, a_{im}]^T$	input weight of the input layer to the i-th hidden layer node
$\beta_i = [\beta_{i1}, \beta_{i2}, \dots, \beta_{im}]^T$	output weight of the i-th hidden layer node
b_i	bias of the i-th hidden layer node
Y	desired output matrix
H	hidden layer output matrix
H^+	Moore-penrose generalized inverse of the H
N_p	Size of the population
P_i	the i-th individual

D	the number of genes on an individual
P_{ij}	the j -th gene on the i -th individual
$p_{ij}^U p_{ij}^L$	the upper and lower limits of the P_{ij}
g	the g -th generation
$v_{r,g+1}$	newly constructed vector in the next generation
F	scaling factor
CR	crossover probability
g_{\max}	maximum number of iterations
$y_i \hat{y}_i$	the actual and predicted values of the suspension force
N_t	total number of training samples
i	suspension winding current
θ	rotor position
Z_i	principal input components
C	the penalty parameter of SVM
γ	the kernel parameter of SVM

References

- Sun, X.; Su, B.; Wang, S.; Yang, Z.; Lei, G.; Zhu, J.; Guo, Y. Performance Analysis of Suspension Force and Torque in an IBPMSM With V-Shaped PMs for Flywheel Batteries. *IEEE Trans. Magn.* **2018**, *54*, 1–4. [[CrossRef](#)]
- Li, X.; Anvari, B.; Palazzolo, A.; Wang, Z.; Toliyat, H. A Utility-Scale Flywheel Energy Storage System with a Shaftless, Hubless, High-Strength Steel Rotor. *IEEE Trans. Ind. Electron.* **2018**, *65*, 6667–6675. [[CrossRef](#)]
- Sun, B.; Dragičević, T.; Freijedo, F.D.; Vasquez, J.C.; Guerrero, J.M. A Control Algorithm for Electric Vehicle Fast Charging Stations Equipped With Flywheel Energy Storage Systems. *IEEE Trans. Power Electron.* **2016**, *31*, 6674–6685. [[CrossRef](#)]
- Takemoto, M.; Suzuki, H.; Chiba, A.; Fukao, T.; Rahman, M.A. Improved analysis of a bearingless switched reluctance motor. *IEEE Trans. Ind. Appl.* **2001**, *37*, 26–34. [[CrossRef](#)]
- Takemoto, M.; Chiba, A.; Akagi, H.; Fukao, T. Radial force and torque of a bearingless switched reluctance motor operating in a region of magnetic saturation. *IEEE Trans. Ind. Appl.* **2004**, *40*, 103–112. [[CrossRef](#)]
- Yu, L.; Zhang, Z.; Shi, Y.; Lu, W. Modeling and Analysis of Suspension Force of a New Bearingless Reluctance Machine With Independent DC Bias Winding. *IEEE Trans. Magn.* **2018**, *54*, 1–5. [[CrossRef](#)]
- Li, F.; Wang, H.; Zhang, F.; Zhang, H. Comprehensive analysis of suspending force for improved bearingless switched reluctance motor with permanent magnets in stator yoke. *CES Trans. Electr. Mach. Syst.* **2018**, *2*, 348–354. [[CrossRef](#)]
- Sun, Y.; Yang, F.; Yuan, Y.; Yu, F.; Xiang, Q.; Zhu, Z. Analysis of a hybrid double stator bearingless switched reluctance motor. *Electron. Lett.* **2018**, *54*, 1397–1399. [[CrossRef](#)]
- Wang, H.; Bao, J.; Xue, B.; Liu, J. Control of Suspending Force in Novel Permanent-Magnet-Biased Bearingless Switched Reluctance Motor. *IEEE Trans. Ind. Electron.* **2015**, *62*, 4298–4306. [[CrossRef](#)]
- Zhu, Z.; Jiang, Y.; Sun, Y. A Novel Bearingless Switched Reluctance Machine with Axial Split Phase Inner Stator Permanent Magnet Structure. In Proceedings of the 2018 IEEE International Magnetics Conference (INTERMAG), Singapore, 23–27 April 2018; p. 1. [[CrossRef](#)]
- Xue, B.; Wang, H.; Bao, J. Design of novel 12/14 bearingless permanent biased switched reluctance motor. In Proceedings of the 2014 17th International Conference on Electrical Machines and Systems (ICEMS), Hangzhou, China, 22–25 October 2014; pp. 2655–2660. [[CrossRef](#)]
- Wang, H.; Liu, J.; Bao, J.; Xue, B. A Novel Bearingless Switched Reluctance Motor With a Biased Permanent Magnet. *IEEE Trans. Ind. Electron.* **2014**, *61*, 6947–6955. [[CrossRef](#)]
- Zhu, Z.; Jiang, Y.; Zhu, J.; Guo, X. Performance comparison of 12/12 pole with 8/10 and 12/14 pole bearingless switched reluctance machine. *Electron. Lett.* **2019**, *55*, 327–329. [[CrossRef](#)]
- Sun, Y.K.; Chen, K.F.; Zhu, Z.Y. A radial force mathematical model of single winding bearingless switched reluctance motors. *Electr. Meas. Instrum.* **2014**, *51*, 31–35.
- Xiang, Q.W.; Zhou, Y.W.; Sun, Y.K.; Ji, X.F. The radial force mathematical model of bearingless switched reluctance motors. *Small Spec. Electr. Mach.* **2013**, *41*, 7–9+13.

16. Xu, Q.S.; Sun, Y.K.; Zhou, Y.W.; Xu, G.H. Finite element analysis of a novel bearingless switched reluctance motor. *Micromotors* **2012**, *45*, 12–15. [[CrossRef](#)]
17. Cao, X.; Li, X.D.; Liu, C.; Deng, Z.Q. Mathematical model of conical bearingless switched reluctance motor based on rotating coordinate System. *Trans. China Electrotech. Soc.* **2018**, *33*, 4029–4036. [[CrossRef](#)]
18. Rong, H.; Huang, G.; Ong, Y. Extreme learning machine for multi-categories classification applications. In Proceedings of the 2008 IEEE International Joint Conference on Neural Networks (IEEE World Congress on Computational Intelligence), Hong Kong, China, 1–8 June 2008; pp. 1709–1713. [[CrossRef](#)]
19. Sun, Y.K.; Yuan, Y.; Huang, Y.H.; Hu, W.H. Multi-objective optimal design of single winding bearingless switched reluctance motor. *Electr. Mach. Control.* **2016**, *20*, 32–39. [[CrossRef](#)]
20. Huang, G.; Zhou, H.; Ding, X.; Zhang, R. Extreme Learning Machine for Regression and Multiclass Classification. *IEEE Trans. Syst. Man Cybern. Part B (Cybern.)* **2012**, *42*, 513–529. [[CrossRef](#)]
21. Richard, G.L. Designing Nonstandard Filters with Differential Evolution. *IEEE Signal Process. Mag.* **2012**, *22*, 25–32. [[CrossRef](#)]
22. Basith, S.; Manavalan, B.; Shin, T.; Lee, G. SDM6A: A Web-Based Integrative Machine-Learning Framework for Predicting 6mA Sites in the Rice Genome. *Mol. Ther. Nucleic Acids* **2019**, *18*, 131–141. [[CrossRef](#)]
23. Wei, L.; Su, R.; Luan, S.; Liao, Z.; Manavalan, B.; Zou, Q.; Shi, X. Iterative feature representations improve N4-methylcytosine site prediction. *Bioinformatics* **2019**. [[CrossRef](#)]
24. Boopathi, V.; Subramaniyam, S.; Malik, A.; Lee, G.; Manavalan, B.; Yang, D. mACPpred: A Support Vector Machine-Based Meta-Predictor for Identification of Anticancer Peptides. *Int. J. Mol. Sci.* **2019**, *20*, 1964. [[CrossRef](#)] [[PubMed](#)]
25. Manavalan, B.; Basith, S.; Shin, T.; Wei, L.; Lee, G. Meta-4mCpred: A Sequence-Based Meta-Predictor for Accurate DNA 4mC Site Prediction Using Effective Feature Representation. *Mol. Ther. Nucleic Acids* **2019**, *16*, 733–744. [[CrossRef](#)] [[PubMed](#)]
26. Basith, S.; Manavalan, B.; Shin, T.; Lee, G. iGHBP: Computational identification of growth hormone binding proteins from sequences using extremely randomised tree. *Comput. Struct. Biotechnol. J.* **2018**, *16*, 412–420. [[CrossRef](#)] [[PubMed](#)]
27. Hou, C.; Yu, X.; Cao, Y.; Lai, C.; Cao, Y. Prediction of synchronous closing time of permanent magnetic actuator for vacuum circuit breaker based on PSO-BP. *IEEE Trans. Dielectr. Electr. Insul.* **2017**, *24*, 3321–3326. [[CrossRef](#)]
28. Yang, A.; Zhuansun, Y.; Liu, C.; Li, J.; Zhang, C. Design of Intrusion Detection System for Internet of Things Based on Improved BP Neural Network. *IEEE Access* **2019**, *7*, 106043–106052. [[CrossRef](#)]
29. Tang, H.; Cao, R.-Z.; Wang, W.; Liu, T.-S.; Wang, L.-M.; He, C.-M. A two-step discriminated method to identify thermophilic proteins. *Int. J. Biomath.* **2017**, *10*, 1750050. [[CrossRef](#)]
30. Hou, J.; Wu, T.; Cao, R.; Cheng, J. Protein tertiary structure modeling driven by deep learning and contact distance prediction in CASP13. *Proteins Struct. Funct. Bioinform.* **2019**, 552422. [[CrossRef](#)]

